Experimental Assessment of Axillary Lymph Node Microwave Tomography Using Anthropomorphic Phantoms

Experimental Assessment of Axillary Lymph Node Microwave Tomography using Anthropomorphic Phantoms

Matteo Savazzi, Olympia Karadima, David O. Rodriguez Duarte,
Jorge Tobon, Francesca Vipiana, Panagiotis Kosmas, Carlos A. Fernandes,
João M. Felício, Raquel C. Conceição

Intended medical application

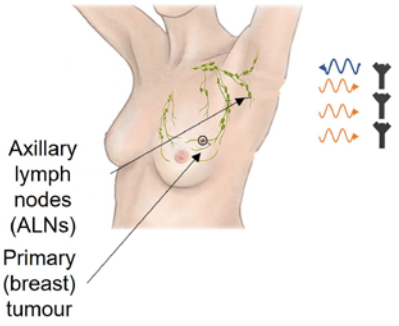

Axillary lymph node diagnosis, for patients affected by breast cancer, using microwave imaging

Developed prototype

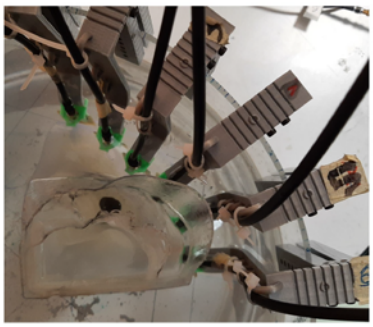

First axillary microwave tomographic system (0.8-2.5 GHz), with an anthropomorphic axillary region phantom

Experimental results

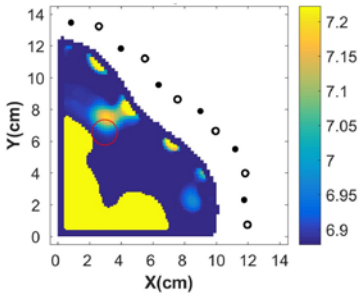

Good ALN detection

Microwave tomographic system for axillary lymph node detection.

Take-Home Messages

- This paper represents the first experimental assessment of microwave tomography for the detection of axillary lymph nodes in patients affected by breast cancer.
- Our microwave tomography system can detect an axillary lymph node placed, in different positions, inside our anthropomorphic phantom of the axillary region.
- The target medical application is the diagnosis of axillary lymph nodes using microwave imaging, which could complement the limited diagnostic information from magnetic resonance imaging and ultrasound.
- This paper presents a microwave tomography setup which could be used as a novel complementary imaging modality for axillary lymph node detection.
- This paper also highlights the challenges of axillary microwave tomography, and proposes a novel method (i.e., two-step angular measurement) to maximize the amount of retrievable information given the limited space for probe placement.

Experimental Assessment of Axillary Lymph Node Microwave Tomography using Anthropomorphic Phantoms

Matteo Savazzi, Olympia Karadima, David O. Rodriguez Duarte, Jorge Tobon, Francesca Vipiana, Panagiotis Kosmas, Carlos A. Fernandes, João M. Felício, Raquel C. Conceição

***Abstract*—We assess the application of microwave tomography (MWT) for the detection of axillary lymph nodes (ALNs) in breast cancer patients. We numerically study the effects of limiting angular view in axillary MWT, as probes can only be placed on a limited arc around the axillary region. We also numerically study the possibility of increasing the amount of retrievable information by acquiring data in two consecutive steps, with a single antenna set in two different angular positions. We finally experimentally test axillary MWT on anthropomorphic phantoms with different levels of anatomical fidelity, and different ALN positions. Our MWT system (0.8-2.5GHz) employs 6 monopole antennas placed on a single transverse plane, facing the axillary region. The reconstruction algorithm implements the distorted Born iterative method, combined with the two-step iterative shrinkage/thresholding for the inversion (DBIM-TwIST). Our numerical results (i) highlight the challenges associated with the limited angular view, and (ii) show that performing two-step angular measurements enhance imaging results, suggesting that rotating the antenna set between consecutive measurements is an effective means to increase the retrievable information in ALN MWT. Our experimental results show that our MWT system can detect an ALN in different positions. To the best of our knowledge this is the first paper to assess ALN MWT in a realistic 3D experimental scenario.**

***Keywords*—axillary lymph node imaging, breast cancer, distorted Born iterative method (DBIM), limited angular information, medical microwave imaging, microwave tomography.**

I. Introduction

BREAST cancer is the most frequently diagnosed type of cancer worldwide, with an incidence of 2.26 million cases in 2020 [1]. Due to their filtering role, axillary lymph nodes (ALNs) are the first organs where possible metastases from breast cancer migrate, which makes ALN diagnosis important for breast cancer staging and for treatment planning [2]. The most accurate method for ALN diagnosis is the sentinel lymph node biopsy (SLNB), which consists of the surgical excision and histological examination of the first regional node (or nodes) to drain the primary tumour. However, SLNB is an invasive procedure which often leads to longer patient recovery, risk of infection and lymphoedema [3], [4]. Pre-surgical and non-invasive medical imaging techniques, such as ultrasound [5] and magnetic resonance imaging [6], [7], are often used to diagnose ALNs, but they have sensitivity and specificity limitations.

M. Savazzi and R. C. Conceição are with the Instituto de Biofísica e Engenharia Biomédica (IBEB), Faculdade de Ciências, Universidade de Lisboa, 1749-016 Lisbon, Portugal (e-mail: mlsavazzi@fc.ul.pt; rcconceicao@fc.ul.pt)

O. Karadima and P. Kosmas are with the Faculty of Natural and Mathematical Sciences, King's College London, Strand, London WC2R 2LS, London, UK (e-mail: olympia.karadima@kcl.ac.uk; panagiotis.kosmas@kcl.ac.uk)

P. Kosmas is also with Metamaterials Inc., Dartmouth, Canada, NS B2Y 4M9

D. O. Rodriguez-Duarte, J. A. Tobón Vasquez, and F. Vipiana are with the Department of Electronics and Telecommunications, Politecnico di Torino, 10129 Torino, Italy (e-mail: david.rodriguez@polito.it; jorge. tobon@polito.it; francesca.vipiana@polito.it).

J. Felício and C. A. Fernandes are with the Instituto de Telecomunicações, Instituto Superior Técnico (IST), Universidade de Lisboa, 1049-001 Lisbon, Portugal (e-mail: joao.felicio@lx.it.pt; carlos.fernandes@lx.it.pt)

J. Felício is also with Centro de Investigação Naval (CINAV), Escola Naval, 2810-001 Almada, Portugal

The possibility of imaging level I ALNs - the ALNs more likely to receive drainage from tumour cells first - using microwave imaging (MWI) is under study in our research group [8], [9], [10], [11], [12], while other authors in the literature also considered such possibility [13]. MWI relies on contrast of dielectric properties between healthy and pathological tissues at microwave frequencies (typically in the 1-10 GHz band), and has the advantages of being non-invasive, low-cost, and potentially translatable into portable devices. In clinical practice, a MWI device for ALN diagnosis could complement the information from other imaging modalities (magnetic resonance and/or ultrasound) and hence improve the sensitivity and specificity of level I ALN diagnosis, possibly avoiding biopsy.

However, axillary MWI presents challenges that are not commonly posed by other medical-MWI systems (e.g., breast and brain MWI devices). In fact, the morphology of the axillary region restricts the measurement domain to a limited arc around the axillary region ($\approx 70^\circ - 90^\circ$ considering the transverse plane) as shown in Fig. 1, significantly limiting the measurement domain, and hence the information available for image reconstruction. Additionally, the concave shape of the axillary region limits the placement of antennas and cables, also restricting the number of probing points in the measurement domain. Level I ALNs are usually located near muscle tissue (with similar dielectric properties) that may have comparable microwave response [10], which poses an additional challenge.

The first experimental study on ALN MWI was conducted in [11], which proposed an air-operating radar-based MWI system to detect ALNs in a fatty homogeneous medium (muscle presence not considered), showing promising results.

The possibility of imaging ALNs with microwave tomography (MWT) was initially numerically assessed in [14] using a simple 2D model of the axillary region. That study investigated the effects of error in prior information on axillary tissue anatomy and dielectric properties, and stressed the importance of having prior information about the fat/muscle interface position.

In this paper, we study - for the first time in a realistic 3D experimental scenario - the application of MWT to the axillary region, which presents several challenges when compared to other anatomical sites commonly studied in medical MWT. We address key aspects of the application, aiming to provide a starting point to anyone approaching axillary MWT in the future. Firstly, we perform a qualitative assessment of the effect of having limited angular view. Secondly, we investigate the possibility of acquiring data from two different angular positions of the antenna set, as a means to overcome the challenges given by limited space for probe placement. Finally, we build an experimental setup and use it to validate our numerical results. Our phantom considers different ALN positions and - as a further element of novelty - the presence of muscle tissue.

II. Axillary Anatomy and Models

This section describes the anatomy of the axillary region, the dielectric properties of axillary tissues, and the axillary models adopted in this work to assess the application of ALN MWT.

A. Axillary anatomy and dielectric properties

Fig. 1(a) shows a representation of the axillary region, where three main tissues can be distinguished: anatomically realistic fat and muscle, and a level I ALN (simply represented as spheroid shape). Based on the anatomical three-level classification of ALNs, level I ALNs are located in the lower part of the armpit, and are usually surrounded by fat tissue. In around 97% of the cases, level I ALNs are the first nodes affected by breast cancer metastases [15], [16]. Their depth (i.e., distance to skin) varies between 14 and 80 mm [17], [12], and correlates to each patient's Body Mass Index (BMI) [18], [19], [12]. Level II ALNs are located between lateral and medial margins of the pectoralis minor muscle, and level III ALNs are medial to the medial margin of the pectoralis minor muscle and inferior to the clavicle [20]. Hence, due to excessive biological tissue attenuation and low contrast against muscles, it is unlikely that level II and level III ALNs can be screened using MWI.

The complex permittivity of axillary tissues at 1.0 GHz is: $\epsilon_r \approx 6 - 1j$ for fat [21]; $\epsilon_r \approx 55 - 17j$ for muscle [21]; $\epsilon_r \approx 56 - 24j$ for ALN [9].

B. Axillary models

We used axillary models derived from the anthropomorphic phantom that we recently developed in [9]. We considered two increasing levels of anatomical accuracy: (i) homogeneous (H) model, consisting of fat tissue only; (ii) multi-tissue anthropomorphic (MTA) model, which is an accurate representation of axillary anatomy, composed of fat and anthropomorphic muscle tissues. Fig. 2 reports pictures of the 3D-printed version of the H and MTA axillary models (i.e., phantoms) used in this study. We then modeled the ALN as a spheroid target, with an equatorial diameter of 16mm and a polar diameter of 12mm.

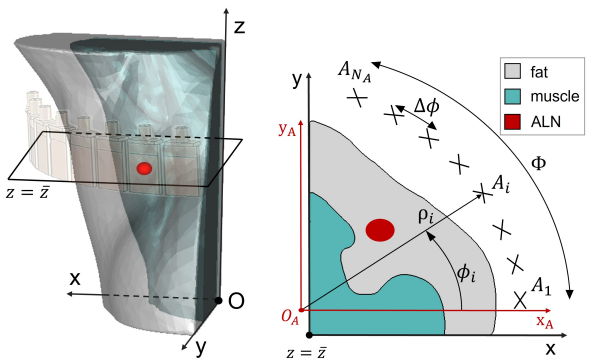

(a) (b)

Figure 1. Representation of the anatomy of the axillary region, and measurement configuration: **(a)** 3D-rendering view; **(b)** cross-sectional view. A level I axillary lymph node (ALN), simply represented with a spheroid shape, is surrounded by fat tissue; at a deeper level (further from the skin) muscle tissue is present. N_A antennas are placed on a single transverse plane $\bar{z}$, facing the axillary region. The axillary model is built from the segmentation of a computed tomographic (CT) image in [9].

For the experimental assessment, we 3D-printed physical phantoms and filled them with liquid tissue mimicking materials (TMMs) made of water, Triton X-100 and NaCl mixtures, as detailed in [9]. We fabricated an ALN TMM as a solidified mixture of polyurethane, carbon black, graphite, and acetone, and we held it in a stable position inside fat TMM using a system of nylon wires tied on specific supports on the 3D-printed phantom parts. We measured the complex permittivity of the TMMs with the open-ended coaxial-probe, and we found that, at 1.0 GHz: $\epsilon_r \approx 6 - 2j$ for fat TMM; $\epsilon_r \approx 53 - 30j$ for muscle TMM; $\epsilon_r \approx 63 - 32j$ for ALN TMM.

We report that our axillary model does not include skin tissue, which simplifies the fabrication of the phantom, but does not impair imaging result. This was verified in [22] and in our numerical analyses - not reported here for the sake of brevity.

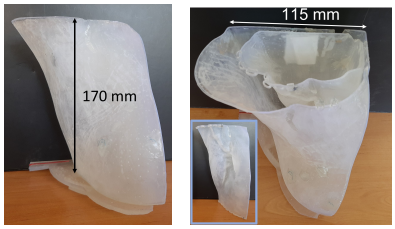

(a) H model (b) MTA model

Figure 2. Representation of the two different axillary models, with increasing level of anatomical fidelity: (a) homogeneous (H) model; (b) multi-tissue anthropomorphic (MTA) model.

III. Microwave tomography system description

This section describes the MWT system adopted in this work and the main design constraints.

Fig. 1 reports a generic representation of the MWT system developed in this paper. In the proposed configuration, the body is immersed in a matching medium, and it is illuminated by N_A antennas placed on a single transverse plane $\bar{z}$, facing the axillary region. Such antenna configuration is convenient given that anatomical constraints (i.e., concave shape of the body) limit the placement of antennas on different planes.

As antennas are placed on a single transverse plane, we may describe the problem at hand referring to the 2D-schematic represented in Fig. 1(b), which illustrates the imaging scenario at an arbitrary $\bar{z}$. Considering the reference system defined in Fig. 1, the antennas are placed on an arc centred in O_A, subtending an angle $\Phi = (N_A - 1)\Delta\phi$, being $\Delta\phi$ the angular spacing between adjacent antennas. We emphasise that - contrary to other MWT applications where the antennas are distributed all around the body [23], [24], [25] - Φ is typically limited to $70° - 90°$ given the morphology of the axilla (imaging problem severely aspect limited), while $\Delta\phi$ is limited by the size of the antennas. Additionally, it has been shown [26] that placing the probes near the imaging domain leads to better reconstruction results in the region close to the border of the imaging domain. This may play a major role in ALN MWT, given the shallow location of the ALN. However, the concave shape of the axillary region hampers the placement of the probes near the body, potentially affecting the performance of the system.

The following subsections detail all different parts of our MWT system.

A. Immersion liquid and frequency range

In MWT, immersion liquids can be used (i) to reduce the size of the antennas, (ii) to increase the system resolution, and (iii) to moderate the mismatch between the system and its model in the imaging algorithm [27]. However, using a lossy medium can cause excessive signal attenuation and deteriorate the reconstruction quality [22]. Additionally, the wavelength reduction is associated to higher degree of non-linearity which challenges the inversion, and requires an increase of the number of probing points in the measurement domain to ensure not missing potential information. In the present study, we adopted glycerol as the immersion liquid, which we identified as a good compromise between the pro and cons listed above. The complex permittivity of glycerol - measured in this work with the open-ended coaxial-probe method - is $\epsilon_r \approx 11 - 9j$ at 1.0 GHz.

Regarding the choice of the frequency bandwidth, previous numerical studies [22] for breast MWT showed that reconstruction accuracy and stability are enhanced when performing a low-frequency reconstruction (e.g., 0.8 GHz) as a prior step to reconstructing data at higher frequencies. We conducted this work in the wide band between 0.8 and 2.5 GHz. The choice of the smaller frequency is related to the minimum acceptable resolution (i.e., $\lambda/4 \approx 26mm$ in glycerol, at 0.8 GHz), while the choice of the maximum frequency is constrained by the maximum number of antennas that could face the axillary region: the canonically used antenna spacing to maximise the amount of retrievable information without redundancies is $\overline{A_i A_{i+1}} = \lambda/2$ [28]. This topic will be further discussed in Sec. IV-B.

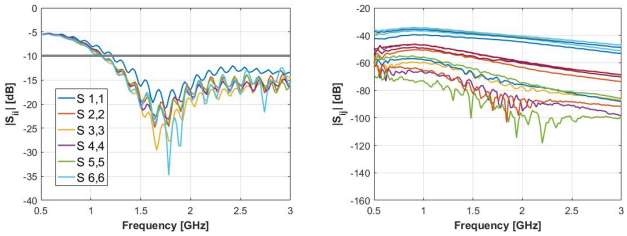

(a) (b)

Figure 3. Scattering parameters of the 6 antennas, measured inside our setup when facing the axillary region phantom filled with fat TMM. **(a)** Reflection coefficients S_{ii} **(b)** Transmission coefficients S_{ij}.

B. Antenna

We adopted wideband monopole antennas (size 30mm x 38mm x 1.6mm), that were already used for medical MWT applications [29]. These antennas have an omnidirectional radiation pattern (in the plane orthogonal to the antenna plane), which represents an advantage as they are best modeled by point sources as the ones we used in our *forward model* (see Sec. III-C). Fig. 3(a) reports the antenna reflection coefficient measured in glycerol: the matching is always below -10 dB in the 1.1-3.0 GHz frequency band, even though we noticed that we can use it at 0.8 GHz. Additionally it has been shown [29], [30] that working outside the main resonance of the antenna (i.e., in a "flatter region" of the $S11$ plot in Fig. 3(a)) can aid tomographic reconstruction.

C. Imaging algorithm

To solve the nonlinear inverse electromagnetic (EM) scattering problem, we employed the general framework of the distorted Born iterative method (DBIM) [31], combined with the two-step iterative shrinkage/thresholding (TwIST) algorithm [32] to solve the linearised system of equations at each iteration. The adopted algorithm was originally proposed for the numerical assessment of breast MWT, using a 2D breast model [22], and experimentally tested for brain MWT in [23].

To solve the *forward problem*, we run the finite-difference time-domain (FDTD) EM-solver with a convolutional perfectly matched layer (CPML) boundary condition, and $1mm \times 1mm$ mesh size, at each DBIM iteration. The 2D-FDTD simulation is excited by point sources with a wideband Gaussian pulse in a transverse-magnetic (TM) mode (i.e., the electric field is perpendicular to $\bar{z}$), centered at the resonance frequency of the antenna. Hence, only one component of E-field (E_z) is modeled.

As a first step after measurements, data calibration is required as the *forward model* computes the electric field (E-field) at the antennas, while the VNA measures the scattering parameters at each port. Additionally, differences

between the computational model and the physical system must be taken into account. In this paper, we adopted the methodology proposed in [33] for data calibration. Such methodology entails (i) measuring a known scatterer ($\mathbf{S}^{known}$) and (ii) computing the E-field ($\mathbf{E}^{known}$) from the same scatterer with the *forward model*. The calibrated E-field for the unknown scatterer ($\mathbf{E}^{patient}_{calibrated}$) is then calculated as:

$$\mathbf{E}^{patient}_{calibrated} = \mathbf{S}^{patient} \frac{\mathbf{E}^{known}}{\mathbf{S}^{known}} \tag{1}$$

where $\mathbf{S}^{patient}$ is the data obtained measuring the unknown scatterer (i.e., patient). Here, we measured $\mathbf{S}^{known}$ and computed $\mathbf{E}^{known}$ using the axillary model without ALN.

We assumed prior knowledge about the morphology and position of torso and muscle to be available. According to this information, we defined the *initial guess* (i.e., the first estimate of the background given as input to our DBIM algorithm) as a 2D cross-section of the axillary region with all organs except the target. We limited the reconstruction of the dielectric profile to the voxels contained in the body (at $z = \bar{z}$).

IV. Numerical assessment

This section focuses on two of the main challenges posed by ALN MWI, namely (i) the limited angular view, and (ii) the space constraints for probe placement. Regarding the first challenge, Sec. IV-A shows the effects of having limited angular view on imaging results. Regarding the second challenge, Sec. IV-B investigates the possibility of acquiring data in two consecutive steps with different angular perspectives. This is a means to increase the probing points in the measurement domain, with the objective of increasing the amount of retrieved information.

A. Effect of limiting angular view

We placed $N_A = 6$ probes (probes 1-6) on the anatomically accessible side of the homogeneous model, while we intentionally placed an extra set of 6 probes (probes 7-12) facing the two - not anatomically accessible - flat back-sides of the model, aiming to obtain a benchmark result to qualitatively assess the effects of having a limited angular domain, which is a major constraint in ALN MWI. Fig. 4(a) illustrates a cross-sectional view of the setup. We embedded an ALN in fatty medium, with ALN-skin distance equal to 23mm (computed from the centre of the ALN). The position of probes 1-6 is given by: $O_A(-21mm, -1mm, \bar{z})$; $\boldsymbol{\rho} = [136, 136, 136, 136, 136, 136]mm$; $\Delta\phi = 15°$. The resulting distance between adjacent antennas is 35mm. The average ($\pm$standard deviation) antenna-body distance is 23($\pm$6)mm, for probes 1-6. Probes 7-12 are spaced 36mm from each other, with constant antenna-phantom distance equal to 23mm.

We collected S-parameters using CST software, discretising the space using an hexaedral mesh, ensuring that the side of each voxel was at maximum $\lambda/20$.

To pursue our investigation, we compared the results obtained considering two subsets of antennas for image reconstruction: (i) antennas 1-12 (i.e., all the antennas), and (ii) antennas 1-6 (i.e., only those on the anatomically accessible side of the axillary model). We reconstructed the images using frequency hopping between 0.8, 0.9 and 1.0 GHz, with 25 DBIM-TwIST iterations per frequency point, in a total of 75 iterations. The choice of the hopping frequencies is later justified in light of the experimental results obtained in Sec. V-B. We chose 25 iterations per frequency as we verified that results tend to be stable when further increasing the number of iterations. Hopping between frequencies means that we firstly reconstructed the lowest frequency, and then used the resulting dielectric map as the *initial guess* to the subsequent (higher) frequency. The reasoning is to initially exploit the stabilizing effect of lower frequencies, and combine it with the finer resolution of higher frequencies, resulting in an enhanced imaging performance as reported in [22].

Fig. 5 reports the images reconstructed at the highest hopping frequency (1.0 GHz) for the two analysed cases. We note that, in the case where we used the signals collected by all the 12 antennas, the target is detected in its correct position in both real and imaginary part of the permittivity. The target detection is more challenging in the case where we considered only the 6 antennas facing the axillary region. As expected, limiting the illumination angle (and the number of probes) affects target detection, which highlights the challenges of the application.

We notice that our algorithm fails to estimate the target dielectric properties within acceptable error (in the real part, the estimated target permittivity is approximately 1.05 times higher than fat permittivity, while it should be approximately 10 times higher). In our previous study [14], we obtained good ALN permittivity estimation when using the same 2D-FDTD in both data generation and image reconstruction, which suggests that the failure to estimate ALN properties may be due to the measurement and model mismatches (i.e., *modelling errors*). We also report that in experimental studies on brain MWT [23], the same DBIM-TwIST algorithm was able to differentiate between targets with different dielectric properties. We hence suspect that the *modelling errors* in axillary MWT are due to: (i) the small size of our target over the z-axis which - after mapping data to the 2D-domain of our model - may result in a reduced response of the target with respect to other organs, and translate in an underestimation of the permittivity; (ii) the different shapes of axilla and brain, and in particular in the non-invariant shape of the axilla over the z-axis (as is almost the case for the brain).

B. Effect of performing two-step angular measurement

Given the limited space available for probe placement in the axillary region, this section proposes a method to maximise the useful retrievable information in axillary MWT, which relies on acquiring data from multiple angular perspectives. We note that the distance between antennas is 36mm, which corresponds to the commonly used $\lambda/2$ antenna spacing at 1.7 GHz. However, the optimal probe spacing depends on several factors, including the measurement precision (dictated by the measurement dynamic range and the signal to noise ratio) and the extension of the measurement domain [34]. In the present case, given the low response of the ALN and

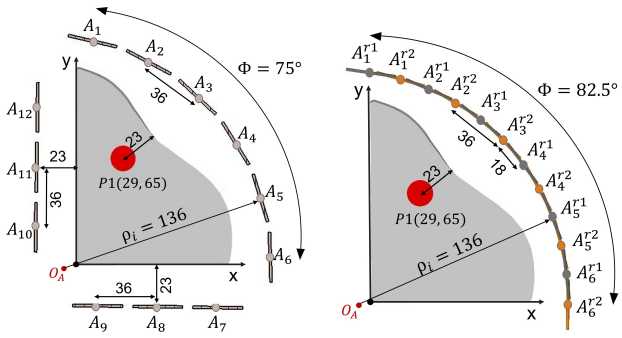

Figure 4. Tomographic setups used for numerical assessment (cross-sectional views at the level of the target). **(a)** Setup used to assess the influence of having limited angular view in axillary MWT: 12 monopole antennas are placed around the homogeneous (H) axillary model. The probes are placed not only in front of the axillary region, but also - in a non-realistic manner - on the back side of the phantom, enlarging the measurement domain. **(b)** Setup used to assess the effect of performing two-step angular measurements: the representation shows the 12 probing points in front of the axilla, obtained as a result of the two rotational position assumed by the 6-antenna set. The apices *r1* and *r2* indicate the two rotational positions assumed by the antennas. Distances are reported in millimeters.

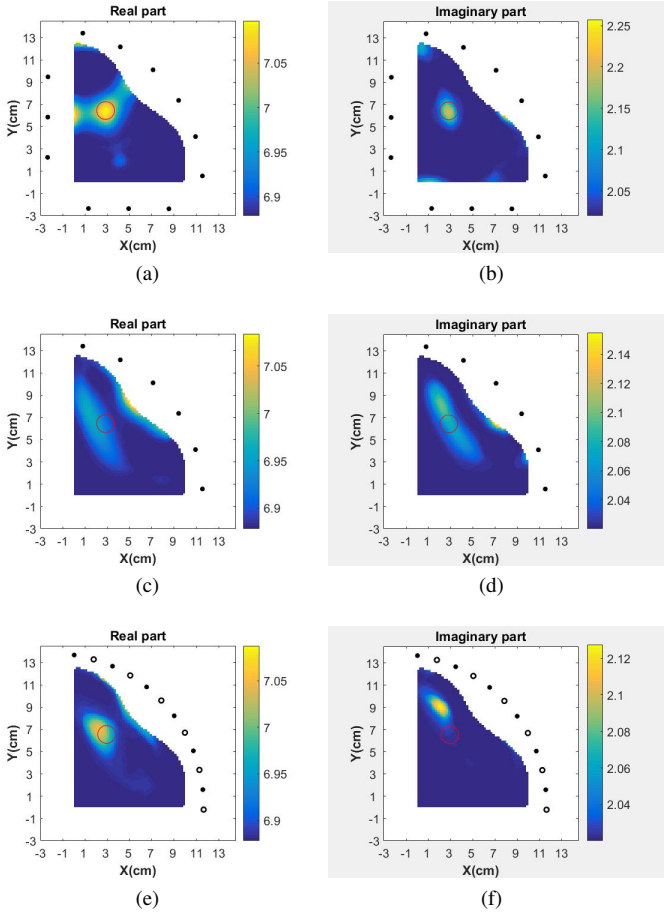

Figure 5. Numerical imaging results obtained with: **(a, b)** 12 antennas, placed all around the model; **(c, d)** only the 6 antennas facing the axillary region; **(e, f)** 6 antennas in two angular positions (as an effect of a $\Delta\phi/2$ phantom rotation). **(a, b)** *vs* **(c, d)** shows the effect of having limited angular view in axillary MWT. **(c, d)** *vs* **(e, f)** shows the effect of increasing the number of probing points in the measurement domain by performing two-step angular measurements. Each image is plotted in the range comprised between the minimum and maximum values of the imaging domain.

the limited measurement domain (limited angular view), we evaluate whether doubling the sampling points will increase the amount of retrieved information.

To pursue such investigation, we adopted the same setup used in Sec. IV-A, excluding antennas 7-12. We collected our data in two consecutive steps, rotating the 6-antenna set by $\Delta\phi/2$ between subsequent measurements. The resulting 12 probing points (6-antenna set in 2 rotational positions) are illustrated in Fig. 4(b), which highlights (different colours) the two rotational positions assumed by the antennas.

As a result, we merged the two obtained 6-by-6 scattering matrices in a single 12-by-12 matrix which - for each frequency - is defined as:

$$S(i,j) = \begin{cases} n.a., & \text{if } i+j \text{ is odd} \\ S^{Ang1}(\frac{i+1}{2}, \frac{j+1}{2}), & \text{if } i \text{ and } j \text{ are odd} \\ S^{Ang2}(\frac{i}{2}, \frac{j}{2}), & \text{if } i \text{ and } j \text{ are even} \end{cases}$$

where $i \in \{1, 2, ..., 12\}$, $j \in \{1, 2, ..., 12\}$; S^{Ang1} and S^{Ang2} are the 6-by-6 scattering matrices measured when illuminating the axillary model with the antenna set in the first and second angular position respectively.

We collected S-parameters using CST software, discretising the space using an hexaedral mesh, ensuring that the side of each voxel was at maximum $\lambda/20$.

Fig. 5(e, f) presents the imaging results obtained using frequency hopping between 0.8, 0.9, and 1.0 GHz, with 25 DBIM-TwIST iterations per frequency point. A comparison between Fig. 5(c, d) and Fig. 5(e, f) suggests that - when acquiring data in two consecutive steps, rotating the antennas - the target detection significantly improves. However, despite good detection in the real part of permittivity (Fig. 5(e)), we observe a localization error (LE) of 26mm in the imaginary part (Fig. 5(f)). We believe that such error is part of the inaccuracies of the inversion process due to the mismatch between the model and the true system. Additionally, a comparison between Fig. 5(b) and Fig. 5(f) suggests that the LE may be due to the limited angular view. We also report that other studies in the literature [23] encountered more difficulties in reconstructing the imaginary part rather than the real part of permittivity. Regarding the significance of the LE, we emphasise that LE = 26mm is deemed acceptable since 26mm (i) corresponds to 0.23 wavelengths (λ=123mm at 1.0 GHz, in fat tissue), and (ii) is comparable to the ALN diameter (16mm) in the analysed plane.

In conclusion, these results suggest that performing measurements at two different angular positions of the antenna set is a good strategy to mitigate space limitations posed by axillary MWT, which motivated us to adopt such approach during our experimental assessment.

V. Experimental Assessment

This section illustrates the developed experimental setup and the results of the measurement campaign performed to test our system, using four different phantom configurations, with increasing level of anatomical fidelity.

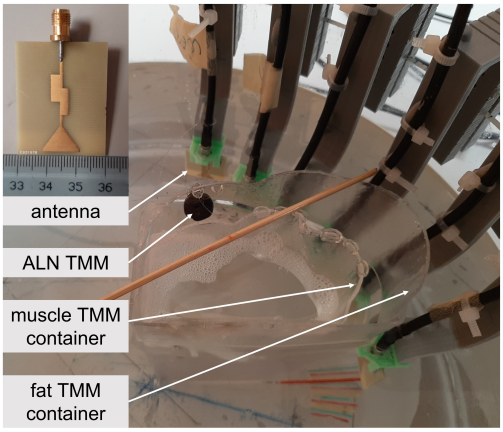

Figure 6. Experimental setup used to assess axillary microwave tomography: 6 monopole antennas are placed covering an angle $\Phi = 75°$ around the axillary region. The phantom is composed of three tissues: fat, muscle, and axillary lymph node (ALN).

A. *Experimental setup*

Fig. 6 illustrates our microwave tomography system, which consists of a cylindrical acrylic tank (diameter $d = 400mm$) filled with glycerol, where we immersed an axillary region phantom, and a set of 6 antennas placed on a single $\bar{z}$ plane facing the axillary region.

Referring to the 2D polar coordinates defined in Fig. 1, the position of the antennas on $\bar{z}$ is given by: $O_A(0, 0, \bar{z})$, $\boldsymbol{\rho} = [135, 125, 115, 120, 125, 120]mm$, and $\Delta\phi = 15°$. The average ($\pm$ standard deviation) distance between antennas and body was of 21($\pm$3)mm (computed on 12 elements, as a result of the two illumination angles), and as uniform as possible across all angular positions.

We combined different ALN positions with different levels of anatomical complexity, which resulted in four different phantom configurations:

1) H-P1: H-phantom with target in position $P1(29, 65, \bar{z})$ (i.e., the same model used for the numerical assessment)
2) H-P2: H-phantom with target in position $P2(63, 44, \bar{z})$
3) MTA-P1: MTA-phantom with target in position $P1$
4) MTA-P3: MTA-phantom with target in position $P3(56, 58, \bar{z})$

We used a Keysight M9804A 6-port vector network analyzer, VNA [35] (maximum nominal dynamic range of 140 dB at 10 Hz IF bandwidth), and we connected each port to a single antenna through two coaxial cables connected in series. Prior to measurements, we performed electronic-calibration at the end of the first cable to remove the influence of the VNA and the cable. We set the VNA output power to the maximum power of 13dBm, while we set the IF bandwidth to 50 Hz, as a compromise between acquisition time and dynamic range. That choice can be understood in light of the low response of the ALN transmitted by the i-*th* probe to the j-*th* probe, which is approximately between -120dB and -100dB.

We initially performed single-frequency reconstructions for all phantom configurations to assess the potential of each frequency. Once the best operating frequencies were identified, we computed the results with frequency hopping within the best-operating frequency band.

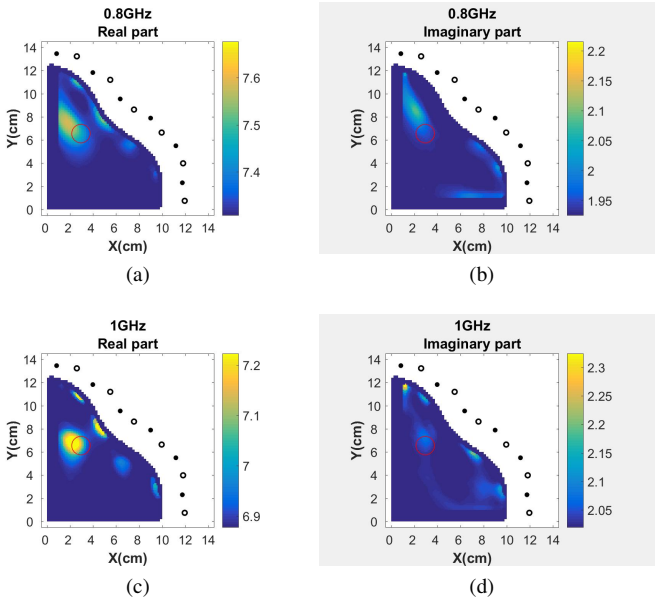

Figure 7. Experimental results obtained reconstructing images at different (independent) frequencies, using the homogeneous phantom whit target in position P1 (H-P1 phantom). **(a, b)** 0.8 GHz, **(c, d)** 1.0 GHz. **(left)** Real part, and **(right)** imaginary part of relative permittivity. Each image is plotted in the range comprised between: (i) minimum value of the image, and (ii) +5% and +15% (for real part and imaginary part respectively) times the median value of the image (which is fat value).

B. *Experimental results*

Fig. 7 presents single-frequency reconstructed images for the H-P1 phantom, at 0.8 and 1.0 GHz. We observe that the ALN is detected in that frequency band (similar results were observed at 0.9 GHz); while for frequencies higher than 1.0 GHz (results not reported due to space constraints), we report that the detection is hindered by clutter presence. This can be explained by the insufficient number of probes that are not able to fully capture the retrievable information at higher frequencies. We also notice that the real part is better reconstructed than the imaginary part, which was also observed in previous studies that adopted the same DBIM-TwIST algorithm [23].

Given that the optimum results are obtained at the 0.8-1.0 GHz frequency range, we reconstructed the images using frequency hopping between 0.8, 0.9 and 1.0 GHz, with 25 DBIM-TwIST iterations at each frequency, in a total of 75 iterations. Fig. 8 presents the imaging results at the highest hopping frequency for the four phantom configurations tested. Referring to H-P1 phantom (Fig. 8(a,b)), we observe that the ALN is detected in its correct position, with improved detection if compared with single frequency reconstructions. The results are consistent when considering a different position of the ALN (H-P2 phantom, Fig. 8(c,d)). The target is detected also when a second known scatterer (muscle) disturbs the propagation inside the axillary region (MTA-P1, MTA-P3 phantoms, Fig. 8(e-h)), which is a promising result. We

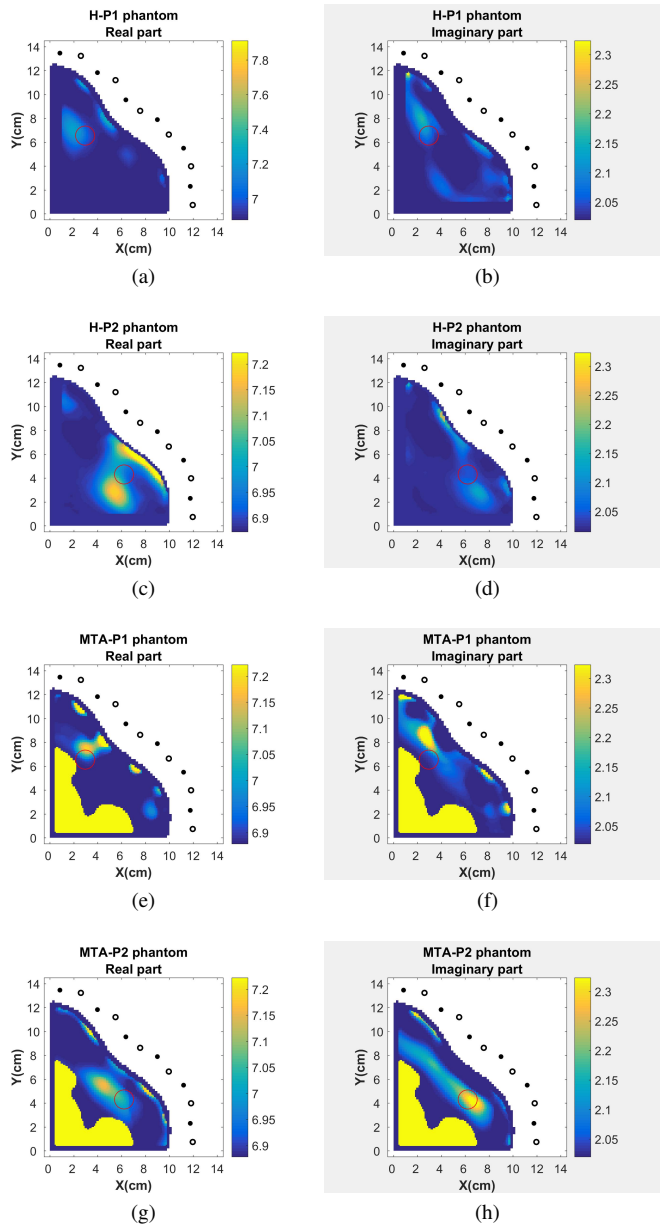

Figure 8. Experimental imaging results obtained with frequency hopping between 0.8, 0.9 and 1.0 GHz, for four different phantoms: **(a, b)** H-P1, **(c, d)** H-P2, **(e, f)** MTA-P1, **(g, h)** MTA-P3. **(left)** Real part, and **(right)** imaginary part of relative permittivity. Each image is plotted in the range comprised between: (i) minimum value of the image, and (ii) +5% and +15% (for real part and imaginary part respectively) times the median value of the image (which is fat value).

also report that we observed such improvement in most of the configurations tested, which suggests that hopping between frequencies is a valid way to improve imaging results while exploring multiple-frequency information. We quantified the LE for each image, and we found that in the worst-case-scenario (imaginary part of permittivity of the MTA-P1 phantom, Fig. 8(f)), LE = 24mm, which is deemed acceptable considering the discussion presented in Sec. IV-B. Overall, we report that more artifacts are present in the experimental results rather than in the numerical results, which may be due, not only to noise and other unknown factors, but also to the presence of polymeric containers in the physical phantom [36].

It should be noted that we obtained these results using a reference model for calibration that corresponds to the “no-target scenario", which is likely to lead to a successful data calibration [33], but would not be feasible in real practice.

VI. Conclusions and Future Work

This work represented the first experimental assessment of MWT technology for the detection of ALNs in patients affected by breast cancer. We tested a prototype (0.8-2.5 GHz) with 6 monopole antennas placed around our anthropomorphic axillary region phantom, immersed in a glycerol bath, and we reconstructed images using the DBIM-TwIST algorithm.

We firstly numerically showed that imaging results deteriorate when placing antennas only on the anatomically accessible side of the axillary model. Secondly, given the limited space available for probe placement near the axillary region, we proposed a method that performs measurements in two subsequent steps, with a single antenna set in two different angular positions, to increase the amount of retrievable information. We demonstrated the effectiveness of our method, and we adopted it for our experimental assessment. Regarding experimental results, these showed that the DBIM-TwIST can detect an ALN in different position in the axillary region, when using simplified (homogeneous) or anthropomorphic (multi-tissue) phantoms, which encourages further studies of the application. However, our algorithm fails to estimate the dielectric properties of ALNs, probably due to the difficulties of our 2D-FDTD solver in modelling the propagation of the E-field in the axillary region. The possibility of using a more accurate 3D model as a forward solver for our algorithm will be studied in future work.

Finally, the data calibration procedure proposed in [37] should be studied in future work as an alternative calibration to the “no-target scenario".

Acknowledgment

This work was supported by the EMERALD project funded from the European Union’s Horizon 2020 research and innovation programme under the Marie Skłodowska-Curie grant agreement No. 764479.

This work is also supported by Fundação para a Ciência e a Tecnologia-FCT, FCT/MEC (PIDDAC) under the Strategic Programme UIDB/00645/2020, UIDB/50008/2020, and 2021.05385.BD.

References

[1] W. H. Organization, “Breast Cancer Fact Sheets,” 2020, [Online]. Available: http://gco.iarc.fr/today.

[2] G. H. Lyman, A. E. Giuliano, M. R. Somerfield, A. B. Benson III, D. C. Bodurka, H. J. Burstein, A. J. Cochran, H. S. Cody III, S. B. Edge, S. Galper *et al.*, “American Society of Clinical Oncology Guideline Recommendations for Sentinel Lymph Node Biopsy in Early-Stage Breast Cancer,” *Journal of Clinical Oncology*, vol. 23, no. 30, pp. 7703–7720, 2005.

[3] H. Rahbar, S. C. Partridge, S. H. Javid, and C. D. Lehman, “Imaging Axillary Lymph Nodes in Patients with Newly Diagnosed Breast Cancer,” *Current Problems in Diagnostic Radiology*, vol. 41, no. 5, pp. 149–158, 2012.

[4] G. H. Lyman, M. R. Somerfield, L. D. Bosserman, C. L. Perkins, D. L. Weaver, and A. E. Giuliano, "Sentinel Lymph Node Biopsy for Patients with Early-Stage Breast Cancer: American Society of Clinical Oncology Clinical Practice Guideline Update," *Journal of Clinical Oncology*, vol. 35, no. 5, pp. 561–564, 2017.

[5] S. M. Dudea, M. Lenghel, D. Vasilescu, and M. M. Duma, "Ultrasonography of Superficial Lymph Nodes: Benign vs. Malignant," *Medical Ultrasonography*, vol. 14, no. 4, pp. 294–306, 2012.

[6] V. E. Mortellaro, J. Marshall, L. Singer, S. N. Hochwald, M. Chang, E. M. Copeland, and S. R. Grobmyer, "Magnetic Resonance Imaging for Axillary Staging in Patients with Breast Cancer," *Journal of Magnetic Resonance Imaging: An Official Journal of the International Society for Magnetic Resonance in Medicine*, vol. 30, no. 2, pp. 309–312, 2009.

[7] P. A. Baltzer, M. Dietzel, H. P. Burmeister, R. Zoubi, M. Gajda, O. Camara, and W. A. Kaiser, "Application of MR Mammography Beyond Local Staging: Is There a Potential to Accurately Assess Axillary Lymph Nodes? Evaluation of an Extended Protocol in an Initial Prospective Study," *American Journal of Roentgenology*, vol. 196, no. 5, pp. W641–W647, 2011.

[8] R. Eleutério and R. C. Conceição, "Initial Study for Detection of Multiple Lymph Nodes in the Axillary Region Using Microwave Imaging," in *9th European Conference on Antennas and Propagation (EuCAP), Lisbon, Portugal*. IEEE, 2015, pp. 1–3.

[9] M. Savazzi, S. Abedi, N. Ištuk, N. Joachimowicz, H. Roussel, E. Porter, M. O'Halloran, J. R. Costa, C. A. Fernandes, J. M. Felício *et al.*, "Development of an Anthropomorphic Phantom of the Axillary Region for Microwave Imaging Assessment," *Sensors)*, vol. 20, no. 17, pp. 49–68, 2020.

[10] M. Savazzi, J. R. Costa, C. A. Fernandes, J. M. Felício, and R. C. Conceição, "Numerical Assessment of Microwave Imaging for Axillary Lymph Nodes Screening Using Anthropomorphic Phantom," in *15th European Conference on Antennas and Propagation (EuCAP), Dusseldorf, Germany.* IEEE, 2021, pp. 1–4.

[11] D. M. Godinho, J. M. Felício, C. A. Fernandes, and R. C. Conceição, "Experimental Evaluation of an Axillary Microwave Imaging System to Aid Breast Cancer Staging," *IEEE Journal of Electromagnetics, RF and Microwaves in Medicine and Biology*, vol. 6, no. 9, pp. 68–76, 2021.

[12] D. M. Godinho, C. Silva, C. Baleia, J. M. Felício, T. Castela, N. A. Silva, M. L. Orvalho, C. A. Fernandes, and R. C. Conceição, "Modelling Level I Axillary Lymph Nodes Depth for Microwave Imaging," *Physica Medica*, vol. 104, pp. 160–166, 2022.

[13] J. Liu and S. G. Hay, "Prospects for Microwave Imaging of the Lymphatic System in the Axillary," in *IEEE-APS Topical Conference on Antennas and Propagation in Wireless Communications (APWC), Cairns, QLD, Australia.* IEEE, 2016, pp. 183–186.

[14] M. Savazzi, O. Karadima, J. M. Felício, C. A. Fernandes, P. Kosmas, and R. C. Conceição, "Effect of Varying Prior Information in Axillary 2D Microwave Tomography," in *16th European Conference on Antennas and Propagation (EuCAP), Madrid, Spain.* IEEE, 2022, pp. 1–5.

[15] U. Veronesi, F. Rilke, A. Luini, V. Sacchini, V. Galimberti, T. Campa, E. D. Bei, M. Greco, A. Magni, M. Merson *et al.*, "Distribution of Axillary Node Metastases by Level of Invasion. An Analysis of 539 Cases," *Cancer*, vol. 59, no. 4, pp. 682–687, 1987.

[16] P. P. Rosen, M. L. Lesser, D. W. Kinne, and E. J. Beattie, "Discontinuous or "Skip" Metastases in Breast Carcinoma. Analysis of 1228 Axillary Dissections." *Annals of surgery*, vol. 197, no. 3, p. 276, 1983.

[17] G. C. Bentel, L. B. Marks, P. H. Hardenbergh, and L. R. Prosnitz, "Variability of the Depth of Supraclavicular and Axillary Lymph Nodes in Patients with Breast Cancer: is a Posterior Axillary Boost Field Necessary?" *International Journal of Radiation Oncology - Biology - Physics*, vol. 47, no. 3, pp. 755–758, 2000.

[18] B. Ludescher, M. Rommel, T. Willmer, A. Fritsche, F. Schick, and J. Machann, "Subcutaneous Adipose Tissue Thickness in Adults - Correlation with BMI and Recommendations for Pen Needle Lengths for Subcutaneous Self-Injection," *Clinical Endocrinology*, vol. 75, no. 6, pp. 786–790, 2011.

[19] M. Houshyari, A. S. Y. Kashi, S. S. Varaki, A. Rakhsha, and E. R. Blookat, "Regional Lymph Node Radiotherapy in Breast Cancer: Single Anterior Supraclavicular Field vs. Two Anterior and Posterior Opposed Supraclavicular Fields," *Electronic Physician*, vol. 7, no. 2, p. 1032, 2015.

[20] S. Kalli, A. Semine, S. Cohen, S. P. Naber, S. S. Makim, and M. Bahl, "American Joint Committee on Cancer's Staging System for Breast Cancer: What the Radiologist Needs to Know," *Radiographics*, vol. 38, no. 7, pp. 1921–1933, 2018.

[21] P. Hasgall, F. Di Gennaro, C. Baumgartner, E. Neufeld, B. Lloyd, M. Gosselin, D. Payne, A. Klingenböck, and N. Kuster, "IT'IS Database for Thermal and Electromagnetic Parameters of Biological Tissues," itis.swiss/database, version 4.0, May 2018.

[22] Z. Miao and P. Kosmas, "Multiple-Frequency DBIM-TwIST Algorithm for Microwave Breast Imaging," *IEEE Transactions on Antennas and Propagation*, vol. 65, no. 5, pp. 2507–2516, 2017.

[23] O. Karadima, M. Rahman, I. Sotiriou, N. Ghavami, P. Lu, S. Ahsan, and P. Kosmas, "Experimental Validation of Microwave Tomography with the DBIM-TwIST Algorithm for Brain Stroke Detection and Classification," *Sensors*, vol. 20, no. 3, p. 840, 2020.

[24] D. O. Rodriguez-Duarte, J. A. Tobon Vasquez, R. Scapaticci, G. Turvani, M. Cavagnaro, M. R. Casu, L. Crocco, and F. Vipiana, "Experimental Validation of a Microwave System for Brain Stroke 3-D Imaging," *Diagnostics*, vol. 11, no. 7, p. 1232, 2021.

[25] S.-H. Son, N. Simonov, H.-J. Kim, J.-M. Lee, and S.-I. Jeon, "Preclinical Prototype Development of a Microwave Tomography System for Breast Cancer Detection," *ETRI Journal*, vol. 32, no. 6, pp. 901–910, 2010.

[26] O. M. Bucci, L. Crocco, and T. Isernia, "Improving the Reconstruction Capabilities in Inverse Scattering Problems by Exploitation of Close-Proximity Setups," *JOSA A*, vol. 16, no. 7, pp. 1788–1798, 1999.

[27] Z. Miao, P. Kosmas, and S. Ahsan, "Impact of Information Loss on Reconstruction Quality in Microwave Tomography for Medical Imaging," *Diagnostics*, vol. 8, no. 3, p. 52, 2018.

[28] O. M. Bucci and T. Isernia, "Electromagnetic Inverse Scattering: Retrievable Information and Measurement Strategies," *Radio Science*, vol. 32, no. 6, pp. 2123–2137, 1997.

[29] J. A. Tobon Vasquez, R. Scapaticci, G. Turvani, G. Bellizzi, N. Joachimowicz, B. Duchêne, E. Tedeschi, M. R. Casu, L. Crocco, and F. Vipiana, "Design and Experimental Assessment of a 2D Microwave Imaging System for Brain Stroke Monitoring," *International Journal of Antennas and Propagation*, vol. 2019, 2019.

[30] D. O. Rodriguez-Duarte, C. Origlia, J. A. T. Vasquez, R. Scapaticci, L. Crocco, and F. Vipiana, "Experimental assessment of real-time brain stroke monitoring via a microwave imaging scanner," *IEEE Open Journal of Antennas and Propagation*, vol. 3, pp. 824–835, 2022.

[31] W. C. Chew and Y.-M. Wang, "Reconstruction of Two-Dimensional Permittivity Distribution Using the Distorted Born Iterative Method," *IEEE Transactions on Medical Imaging*, vol. 9, no. 2, pp. 218–225, 1990.

[32] J. M. Bioucas-Dias and M. A. Figueiredo, "A New TwIST: Two-Step Iterative Shrinkage/Thresholding Algorithms for Image Restoration," *IEEE Transactions on Image Processing*, vol. 16, no. 12, pp. 2992–3004, 2007.

[33] M. Ostadrahimi, P. Mojabi, C. Gilmore, A. Zakaria, S. Noghanian, S. Pistorius, and J. LoVetri, "Analysis of Incident Field Modeling and Incident/Scattered Field Calibration Techniques in Microwave Tomography," *IEEE Antennas and Wireless Propagation Letters*, vol. 10, pp. 900–903, 2011.

[34] O. M. Bucci, L. Crocco, and R. Scapaticci, "On the Optimal Measurement Configuration for Magnetic Nanoparticles-Enhanced Breast Cancer Microwave Imaging," *IEEE Transactions on Biomedical Engineering*, vol. 62, no. 2, pp. 407–414, 2014.

[35] "M980xA Series PXIe Vector Network Analyzer," Website: https://www.keysight.com/ie/en/assets/3119-1014/data-sheets/5992-3596.pdf, [Online PDF]. Accessed on 10/2022.

[36] T. Rydholm, A. Fhager, M. Persson, S. D. Geimer, and P. M. Meaney, "Effects of the Plastic of the Realistic GeePS-L2S-Breast Phantom," *Diagnostics*, vol. 8, no. 3, p. 61, 2018.

[37] S. Tu, J. McCombe, D. Shumakov, and N. Nikolova, "Fast Quantitative Microwave Imaging with Resolvent Kernel Extracted from Measurements," *Inverse Problems*, vol. 31, no. 4, p. 045007, 2015.